

RESEARCH PAPER

Bioimaging comparison between synthesized carbon quantum dots and nanodiamonds

Somayeh Marouzi¹, Shirin Sammak², Kayvan Sadri³, Majid Darroudi^{3*}

¹ Department of Pharmaceutical Biotechnology, School of Pharmacy, Mashhad University of Medical Sciences, Mashhad, Iran

² Department of Medical Biotechnology and Nanotechnology, Faculty of Medicine, Mashhad University of Medical Sciences, Mashhad, Iran

³ Nuclear Medicine Research Center, Mashhad University of Medical Sciences, Mashhad, Iran

ABSTRACT

Objective(s): Scientists have been focused on finding access to the potential of different materials, incredibly natural substances. This work compared two categories of nanoscale materials based on carbon sources, including carbon quantum dots (C-QDs) and detonation nanodiamonds (DNDs).

Materials and Methods: The hydrothermally synthesized C-QDs from *Salvia Hispánica* L. and DNDs were compared through physicochemical tests such as ultra-violet spectrophotometry (UV-Vis), Fourier transform infrared (FT-IR), X-ray diffraction (XRD), and field emission scanning microscopy (FESEM). Then, we investigated their cytotoxicity and biocompatibility on HEK293 and HepG2 cell lines, respectively. To focus on nanoparticle biodistribution and shelf life throughout the in vivo studies of rats, C-QDs and DNDs were labeled by Technetium (99mTc) radioisotope for tracking purposes.

Results: The characterization and cytotoxicity outcomes of C-QDs and DNDs confirmed both cases' relative intrinsic similarity and non-toxicity, which also gained permission to enter the in vivo studies of rats.

Conclusion: According to biodistribution assessments, despite the slight differences between their biological properties, C-QDs, and DNDs exhibited different bioaccumulation tendencies toward organ selection.

Keywords: Carbon quantum dots; Technetium; Nanodiamonds; Hydrothermal synthesis; Bioimaging

How to cite this article

Marouzi S, Sammak Sh, Sadri K, Darroudi M. Bioimaging comparison between synthesized carbon quantum dots and nanodiamonds. *Nanomed J.* 2025;12(3):529-545 DOI: 10.22038/nmj.2025.81851.2037

INTRODUCTION

Nowadays, nanotechnology is recognized as an efficient technique for the practical exertion of materials in various fields of scientific societies such as medicine and industry. The "green synthesizing" methods of nanotechnology as a biocompatible, fast, and cost-effective approach for producing biodegradable and non-toxic nanomaterials have been considered by scientists in the last decade [1]. Carbon is recognized as an essential element in all organisms, including plants and animals since the abundance and diversity of carbon allotropes led to the creation of structures with unique properties [2, 3]. Nano-scale carbon structures can be referred to as forms of sp^2 , such

as carbon fullerenes and carbon nanotubes (CNTs) [4], while sp^3 carbon nanomaterials are labeled as nanodiamonds (NDs) and carbon quantum dots (C-QDs) [5, 6]. Nanoscale is known for increasing the surface-to-volume ratio by reducing the dimension of materials into atom size [7]. In this regard, different quantum structures can be enumerated, such as quantum wells (reduction of one dimension and enlargement of two other dimensions) [8], quantum wire (reduction of two dimensions and stability of the third dimension) [9], and creation of a quantum point (reduction of three dimensions) with unique behaviours [10]. Semiconductor nanocrystals or quantum dots with dimensions <10 nm can bind to polymers, organics, and biological compounds because of various functional groups on their surfaces [11]. In addition, adjustable levels, optical stability,

* Corresponding author: Email: Darroudim@mums.ac.ir

Note. This manuscript was submitted on August 11, 2024; approved on September 28, 2024.

high biocompatibility, and very little or zero toxicity resulted in extending the attention of scientists for performing quantum dots-based research. Following, exploiting the potential of natural materials in the form of C-QDs facilitated specific applications such as bioimaging [12, 13], targeted drug delivery [14], photocatalyst [15, 16], and biosensor [17, 18], as well as simple, high sensitive [19], and cost-effective approach for biodistribution [20]. Generally, the production methods of C-QDs implicate “top-down” and “bottom-up” techniques [21]. For example, “crushing” carbon structures according to the top-down procedure produces specific structures such as graphite, graphene, and carbon nanotubes [22], despite the top-down methods being applicable for further controlling the location and placement of quantum dots in electronic circuits. However, the mass production of C-QDs under controlled conditions, including temperature changes or reaction stabilizers, converts metal salts into uniform crystals through a bottom-up method. For example, “bottom-up” methods include the arc discharge method for fabricating nanoparticles under harsh conditions, the colloidal synthesis and carbonization of small molecules (carbohydrates, organic acids, and amines) or polymer precursors in relatively simple and gentle conditions such as hydrothermal procedures [23], ultrasonic reactions [24], and microwave decomposition [25, 26]. Also, related reports confirmed the spherical morphology and presence of sp^3 molecular orbitals with amorphous structures or nanocrystals with sp^2 carbon clusters within C-QDs in diamond-like constructions [27]. Diamond nanoparticles with compressed carbon core and carbon-carbon covalent bonds are known as one of the CNT allotropes [28]. Crystal octagonal architectures in the size of <15 nm, which contain interchangeability for exchanging two types of bonds in molecular orbitals (sp^2 and sp^3), can cause flexibility in the surfaces of unstable electrons of diamond nanoparticles [29, 30]. Particular sedimentary layers, meteorites, and crude oil are the natural sources of diamond nanoparticles. Meanwhile, different synthesizing techniques are used in laboratories, such as laser erosion [31], high-pressure ball mill [32], autoclave synthesis of supercritical liquids [33], graphite ion irradiation [34], sonication cavitation [35], and explosives or chemical vapor deposition (CVD) [36]. The synthesis of diamond nanoparticles by blasting soot

residues from explosives with a size of less than 10 nm depends on the conditions and capacity of the exerted cooling chamber in the explosion, which involves CO_2 , weather, etc. [37]. The significant advantages of diamond nanoparticles include a high surface-to-volume ratio, surface adjustment, optical activity, mechanical properties, and simple application [38]. Therefore, these can be exerted for clinical applications such as cancer treatment, gene transfer, and tracking, as well as various biomedical implementations in bioimaging, drug delivery, protein separation, and binding to biological molecules [39, 40].

Radionuclides are not only important for therapeutic and diagnostic applications due to their radioactive nature, but they are also recognized as effective cytotoxic agents worldwide. The therapeutic purposes of α - and β -radioisotopes, where cell damages are inevitable as a result of ionizing radiation, can be exerted through different mechanisms such as reactive oxygen species, single-stranded and double-stranded fractures, and inhibition of repair mechanisms [41]. The DNA products have been under experimental trials by the medical community, while radio drugs such as γ and β^+ are used in imaging techniques for diagnostic purposes in organisms. In this regard, the induced cell damage caused by ionizing radiation due to the lack of focus on cancerous tissues or tumors, which reduces the applied impact on targeted tissue, is considered a challenge for nuclear and clinical medicines.

Drug delivery systems are designed to focus on specific tissues [42]. Numerous reports indicated decreased systemic toxicity and increased practical efficacy during treatment [43, 44]. Reducing the dosage of radiopharmaceuticals for each patient can offer benefits such as decreasing the rate of biological damage caused by ionizing radiation, reducing costs, and increasing the quality of diagnostic images. Therefore, optimizing the administration of radioisotope doses is a significant and essential principle of safety in worldwide medical diagnosis treatments [45, 46]. Nuclear medicine imaging studies are performed by the usage of radioisotopes (^{131}I , ^{111}In , ^{201}Tl , ^{18}F , ^{99m}Tc , and ^{67}Ga) by light-based techniques, which provide the opportunity to evaluate the penetration and absorption coefficient of ligands attached to radiopharmaceuticals, and *in vivo* persistence in various organs [47, 48]. Technetium (^{99m}Tc) is known as the most widely available and

used radiopharmaceutical nuclear medicine, known to contain a physical half-life of 6 h by emitting gamma rays at 140 Kev. In addition, it can obtain excellent images compared to similar radioisotopes due to the lack of causing any effects as the emitted radiation on organs leaves the body [49, 50]. We have evaluated a comparative biological distribution by injecting C-QDs and NDs in rats, including the synthesized product from chia seeds and purchased diamond nanoparticles labeled with a ^{99m}Tc radioisotope. Therefore, this assessment aimed to compare relatively similar nanoparticles for targeted and safe drug delivery purposes. In addition, the characteristics obtained were analyzed using the results of FT-IR, zeta potential, XRD, photoluminescence, UV-Vis spectrophotometry, and transmission electron microscopy (TEM) studies. In the following, we examined the cytotoxicity by performing the quality control test of nanoparticles labeled with ^{99m}Tc radioisotope and using *in vivo* imaging through the intravenous injection of rats to design an intelligent drug delivery system.

MATERIALS AND METHODS

Materials

This work used Latin American chia seeds as a plant source for performing the green synthesis of carbon quantum dots (C-QDs). At the same time, detonation nanodiamonds (DNDs) were purchased with 99% purity from a company in China. The materials used in the cytotoxicity examination included culture medium powder DEMEM (Gibco), MTT, and cell culture flask (T25, T75), which were acquired from Sigma-Aldrich Company, USA. Additionally, a kidney cell line (HEK293) and a liver

cancer cell line (HepG2) from Ferdowsi University Cell Bank were provided (purchased from Pasteur Institute in Tehran). Radionuclide (^{99m}Tc), supplied by Pars Isotope Company (PIC) of Tehran, is affiliated with the Atomic Energy Organization. The employed materials, including SnCl_2 as the reducing agent, silica gel paper, Ketamin and Xylazine (10%, 2%), Whatman paper, hydrochloric acid, and acetone, were all provided from Merck in Germany.

Methods

In this work, the C-QDs were synthesized from the plant source of chia seeds through a hydrothermal green synthesizing approach. In brief, the obtained mucilage from 1.0 g of chia seeds at a specified temperature and time (60 °C, 2 h) was transferred to an autoclave Teflon container for four hours at 180 °C. After gradual cooling to room temperature, the solution was subjected to screening steps such as ultrasonic baths, centrifugation at 10,000 rpm for 15 min, and the final syringe filtration (0.22 μm). The obtained light brown solution was stored in a refrigerator in the dark at 4°C. Subsequently, 20 mg of (DNDs), purchased from Henan Hengxin Ultrahard Material Co. were dispersed in deionized water by an ultrasonic bath by previous studies. Once the prepared suspension was stored in a refrigerator for 24 hours, the supernatant was transferred to a rotary solvent evaporator to remove the solvent. The assessments were performed at a concentration of 1000 mg/ml. The synthesizing steps of C-QDs are schematically exhibited in Fig. 1.

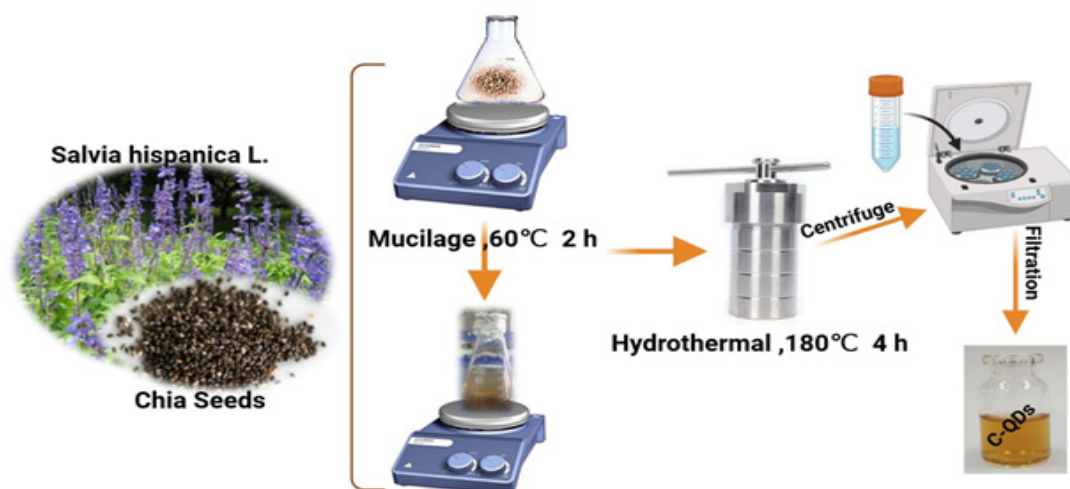


Fig. 1. The schematic of the C-QDs synthesis procedure.

Characterization

The functional groups of C-QDs and DNDs were determined by FTIR (Avatar 370, USA) at a resolution of 4.0 cm^{-1} and a scan number of 4 throughout the $400\text{--}4000\text{ cm}^{-1}$ range. We also evaluated the crystallographic structure through the XRD Panalytical Co. Holland with a $\text{K}\alpha_1$ copper lamp at a wavelength of 0.154 nm . The optical analysis of nanoparticles was performed using UV-Vis spectrophotometry and F-2500 spectrophotometer (Hitachi) due to their small sizes and the presence of functional groups on their surface. The data was collected at room temperature and recorded at a cell length of 10 mm , a bandwidth of 1.5 nm , and a scan speed of 400 nm/min . As it is known, luminescent compounds are crucial for systemic studies, concentration assessment, and labeling of other chemical molecules or particles since they can absorb light at specific frequencies. In this regard, we exerted luminescence-based spectrofluorometers with a scanning speed of 1200 nm . They were equipped with 1.0 cm quartz, which consisted of source sections, excitation wavelength selector, emission wave selector, sample cell, detector, and processor. In addition, the ζ -potential and DLS of C-QDs and DNDs, in both single and labeled forms, were measured at $25\text{ }^\circ\text{C}$ by applying dynamic light scattering SZ-100z and ζ -analyzer instrument (Horiba Co., Japan). The morphology and size of synthesized C-QDs were examined through the results of TEM with a magnification of (80–500,000) times by Zeiss Leo 912 AB (Germany). In preparation for the synthesized C-QDs, a few product drops were dried on a copper-carbon film at room temperature. The morphology and surface structures of the synthesized C-QDs were examined three-dimensionally in high resolution via probe-C-QDs interaction on a mica sheet, which required the usage of AFM (Atomic force microscopy) Brisk model of Ara Research Company (Iran) with a maximum scanning range ($4\text{ }\mu\text{m}$) and resolution of (0.1 nm). Surface specifications and internal microstructure of DNDs were obtained using the FESEM results, which were obtained with an MIRA3 model (TESCAN, Czech). The assessment of DNDs implicated their coating with a FESEM microscope on a metal substrate (20 kW) to be vacuumed (three minutes).

Cytotoxicity assessment

In this section, we performed screening

studies on the cytotoxicity of synthesized CQDs from chia seed extract and the prepared DNDs suspension on HEK293 and HepG2 cell lines, respectively. In summary, the appointed cell lines were cultured under standard conditions to be incubated for 24 h in the presence of necessary materials for cell culturing, such as bovine serum $\%10$ and penicillin-streptomycin. (5×10^3) cells were settled in each well and incubated for 48 h at a concentration range of $0\text{--}500\text{ }\mu\text{g/ml}$. A fresh culture medium containing $500\text{ }\mu\text{l}$ with 5 mg/ml MTT reagent was replaced and incubated for 4 h . At this point, DMSO was added to the solution of the well to remove the reduced crystals by cells. The optical absorption of the plate was read at 570 nm using an ELISA reader (Winooski, VT, USA), and the mean $\pm\text{SD}$ was calculated to determine the amount of toxicity and percentage of cell viability. The inhibitory concentration (IC_{50}) obtained from the outcomes of the MTT was used in the $62.5, 125,$ and $250\text{ }\mu\text{g/ml}$ range for C-QDs and DNDs, respectively. For this purpose, an incubation process was conducted in the presence of $500\text{ }\mu\text{l}$ of solution containing Annexin V-FITC/PI dye for 15 min . As the last step, the cell lines were evaluated by flow cytometry.

Radiolabeling of C-QDs/DNDs- $^{99\text{m}}\text{Tc}$

The application of biocompatible carbon sources has always been considered for achieving the goals of centralized diagnosis and treatment. The studied nanoparticles (C-QDs, DNDs) were labeled with a technetium radioisotope obtained from the ion exchange process (Molybdenum-technetium generator) in sodium pertechnetate. 2.0 mg of Tin-chloride II (reducing agent) was added to 2.0 ml of 1.0 M HCl to form a solution of $\text{SnCl}_2 \cdot 2\text{H}_2\text{O}$. Then, $1000\text{ }\mu\text{l}$ of nanoparticles with a concentration of 1000 ppm and $100\text{ }\mu\text{l}$ of aqueous tin-chloride solution were poured into a separate microtype along with $500\text{ }\mu\text{l}$ of $3\text{ mCi }^{99\text{m}}\text{Tc}$. As the last step, the microtube was incubated at 1400 rpm for 20 minutes at room temperature [51-53].

In-vitro stability of labeled C-QDs/DNDs- $^{99\text{m}}\text{Tc}$ Quality control

We utilized the instant thin layer chromatography (ITLC) method to evaluate the efficacy of nanoparticle labeling with the $^{99\text{m}}\text{Tc}$ radiopharmaceutical. This assay required the usage of two separate media, human serum

(250 μ l) and double distilled water (500 μ l) that contained labeled nanoparticles in the volumes of 100 μ l and 250 μ l, respectively. Then, the staining (5 μ l) was performed at a distance of 0.5 cm above the edge of silica gel paper (110 cm) in the form of a fixed phase. The stained silica gel strips were placed separately in tanks containing 85% methanol and acetone (as the mobile phase). Meanwhile, the wet paper strip was divided into three parts to be separately put inside the sample site for reading the γ -ray. The amount of γ -rays at intervals of 0, 4, 1, and 24 h was monitored by the γ -counter (DL 100) [51].

Cell binding

This section included the assessment of the cell binding of ^{99m}Tc -labeled nanoparticles (C-QDs, DNDs) throughout HEK293 and HepG2, respectively. Each well of the six well-plate contained 1×10^6 cells for performing a cell culturing process for 72 h by standard conditions. ^{99m}Tc -labeled nanoparticles were added to the cell wells at the two concentrations of 90, 30 $\mu\text{g}/\text{ml}$ (three replications) to be incubated for 3h. Once the supernatant was removed, the cells were washed with PBS three times to be transferred to anti-gamma tubes. The activity of cells trypsinized, and the supernatant was read separately by a γ -counter device while focusing on the percentage of removal or binding of ^{99m}Tc conjugated nanoparticles throughout the cell lines.

Animal studies

This study required the application of Wistar rats with an approximate weight of 250 g, which were selected from the animal house of the School of Medicine (MUMS) under controlled conditions, including temperature and light cycle (24°C, 12

h), respectively, starting from natural light under ethical committee's protocol ref. IR.MUMS.MEDICAL. REC. 1399. 663. *In vivo* studies were conducted with the approval of the research ethics committee and compliance with ethical principles.

In-vivo biodistribution analysis of the labeled ^{99m}Tc -C-QDs/DNDs

We evaluated the conjugated bio-distribution of nanoparticles (C-QDs, DNDs) labeled with ^{99m}Tc on the rats under controlled conditions. In this point, three groups with time intervals of 1, 4, and 24 h, along with three replications of rats, were injected with 200 μ l of ^{99m}Tc -(C-QDs/DNDs) through their lateral tail vein [54]. Then, each group's rats were sacrificed according to their injection time. In addition to blood, other organs were weighed separately and accurately and then read using a γ -ray counter. The ^{99m}Tc -(C-QDs/DNDs) activity of each tissue (dose accumulated in each tissue) was presented as the percentage of injected dose (%ID)/g of tissue [55].

Bioimaging analysis of the labeled ^{99m}Tc -(C-QDs/DNDs)

The usage of a γ -camera performed rat imaging study (according to national rules), Siemens Double model (Germany), and the application of intraperitoneal injected (130 μL xylene and 230 μL ketamine) rat for 24 h, which was selected from the experimental group. The images of ^{99m}Tc -(C-QDs/DNDs) conjugate injection at 6 and 24 h can be observed as posterior and anterior images.

RESULTS AND DISCUSSIONS

FTIR

to the FTIR spectrum presented in Fig. 2, structural analysis of chia extract, synthesized

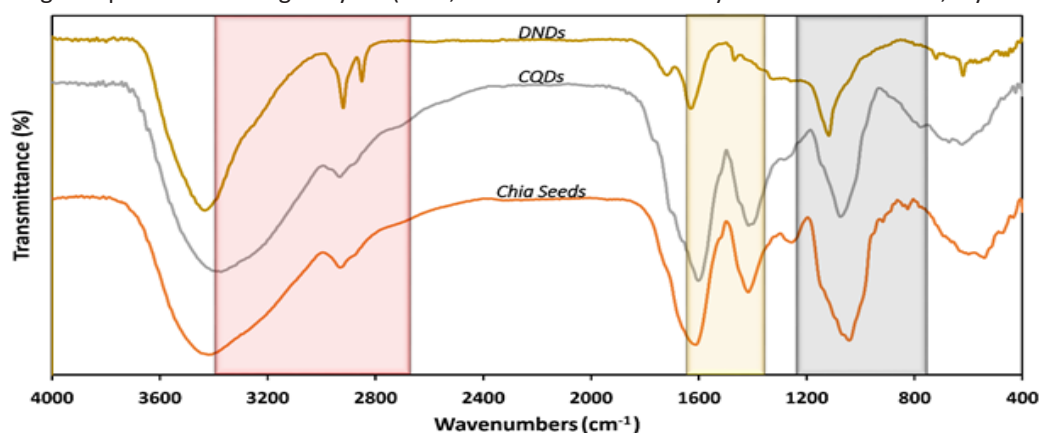


Fig. 2. The FTIR spectra relate to the functional groups in chia extract, C-QDs, and DNDs.

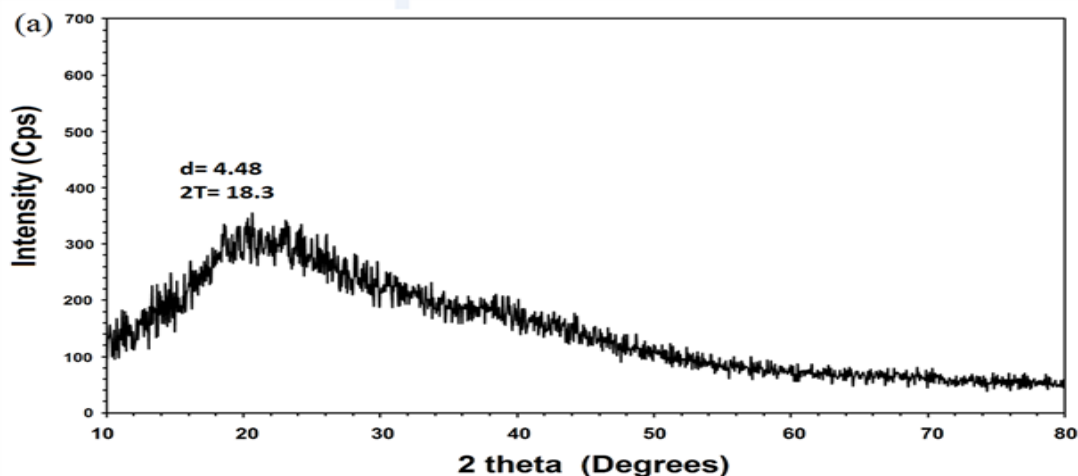
powder, and purchased DNDs were studied to determine their characteristics. The detected peak at 3420 cm^{-1} is related to the chia seed extract and represents the tensile vibration of OH and H bonds in the COOH, and N-H groups, confirming the presence of hydroxyl groups on the surface. This peak was recorded in the C-QDs sample after being synthesized towards lower wavelengths with a peak index of 3373 cm^{-1} . Also, some alterations were observed in the 1611 and 1258 cm^{-1} peaks of chia seed extract after being synthesized, with the recorded peaks at 1596 and 1282 cm^{-1} , respectively, caused by the vibrational changes of water molecules. The mentioned peaks are related to the vibration of alkoxy groups (aromatic compounds), including C=C and C-O. Those with the peak indices of 1070 and 1041 cm^{-1} in the FTIR spectrum of chia seed extract were determined as the single peak (1075 cm^{-1}) of the C-QDs sample while affirming the C-O tensions and C-H bending vibrations outside the plate. The adsorption was observed through the peaks 669 and 620 cm^{-1} as they were created by angular deformations outside the aromatic rings (C-H) in the FTIR spectrum of the synthesized C-QDs sample [56].

In general, the outcomes of FTIR spectral analysis for chia seed extract and the synthesized form (C-QDs) were consistent with that of the zeta potential analysis. Specific changes, such as decreased size, increased solubility due to the presence of multiple functional groups (-COOH, -OH, and -NH₂), and a negative charge caused by the zeta potential, led to the uniform dispersion of C-QDs in the aqueous solution. Therefore, the synthesized C-QDs, through the hydrothermal method (green synthesis) from plant sources, can be exerted as biodegradable sources for biological imaging due to their potential and natural

function at the atomic level. Subsequently, the stretching vibrations of N-H and O-H groups can be seen in the 3433 cm^{-1} regions on the surface of DNDs. In contrast, the activity of the stretching vibrations due to C-H groups (symmetric and asymmetric) can be attributed to 2929 and 2850 cm^{-1} . The peaks detected at 1717 cm^{-1} and 1629 cm^{-1} contain stretching vibrations related to C=O carbonyl groups. The $700\text{-}1470\text{ cm}^{-1}$ regions include the vibrations of different bonds (C-O, C-C, C-H, and C-N) and contain specific information (fingerprint region) about the chemical structure of DNDs [57]. FTIR spectroscopy results of DND samples confirmed their small sizes along with the presence of numerous functional groups. The presence of functional groups (-CH₃ and -OH) on the surface of synthesized CQDs and purchased DNDs can make them suitable candidates for drug delivery, biosensors, and bioimaging.

XRD

Accordingly, the processing and counting of scattered X-rays, obtained by dealing with the structural angles of information materials such as graphite, indicates the distances between the layers and the degree of purity [58]. The graphite pattern of C-QDs bandwidth of 18.3° introduced an amorphous structure. The distances between the 4.84 layer at the 18.3 -degree peak were signs of a compatible structure with the graphite pattern. The XRD results indicated the carbonization of chia seeds by displaying the purity of C-QDs while confirming the excellent solubility of C-QDs solution as well due to the presence of hydrogen bonds (-CH, and -OH) on their surfaces and electron transmission, such as π - π^* , based on the obtained FTIR spectrum. Fig. 3 exhibits the obtained XRD spectrum from the crystal structure



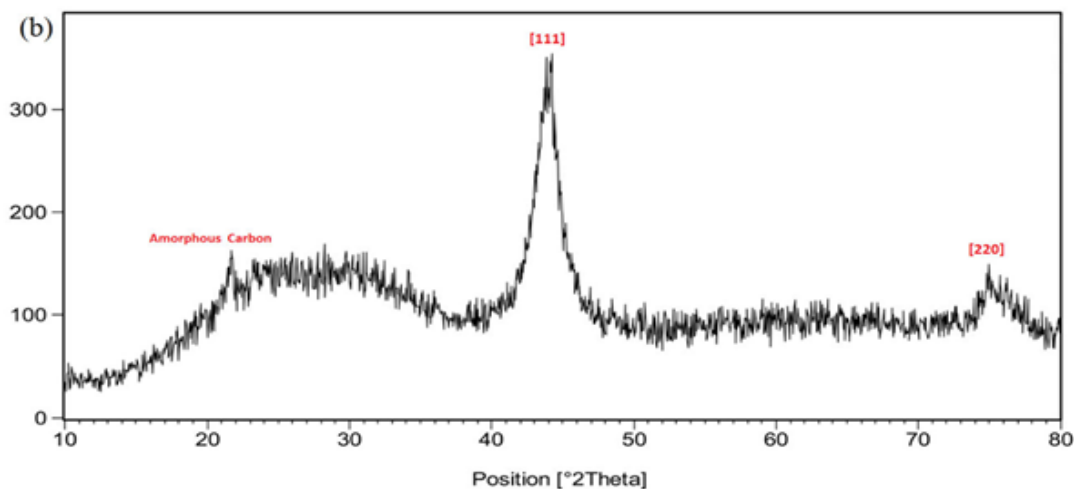


Fig. 3. XRD pattern of synthesized (a) C-QDs and (b) DNDs.

of C-QDs. The observed signal is related to the amorphous carbon of DNDs and seems to agree with the SP^3 molecule orbitals in C-QDs graphite. The miller's indexes of 111 and 220 were parallel with the diamond atomic plates in JCPDS card pattern 06-0675, while the scattering intensity 111 corresponded to graphite 002 [59, 60]. Hence, the XRD results confirmed the small particle size, crystal structure, and high purity degree of the purchased DNDs.

Optical properties

The presented spectrum diagram in Fig. 4a displays the absorption peak related to the transfer of $\pi-\pi^*$ (C=C bonds) with a peak of 280 nm and a shoulder extension towards the range

of 600 nm. Also, carbonyl bonds (C=O) with $n-\pi^*$ transitions were observed in the range of 350-370 nm in small combs that confirmed the formation of C-QDs. Fig. 4b shows the placement of synthesized C-QDs solution under sunlight and UV light (365 nm). The fluorescent radiative properties of C-QDs are due to their small particle size and multiple surface functional groups. Hence, with ultraviolet radiation at 365 nm, the color of the sample was turned from yellow amber to light green [61]. According to the FTIR and XRD spectra, the green radiance of the C-QDs solution and the absorption spectra obtained from the UV-Vis affirmed the size of C-QDs and excellent aqueous solubility. Subsequently, Fig. 4c provides data on examining visible and ultraviolet spectroscopy in the range

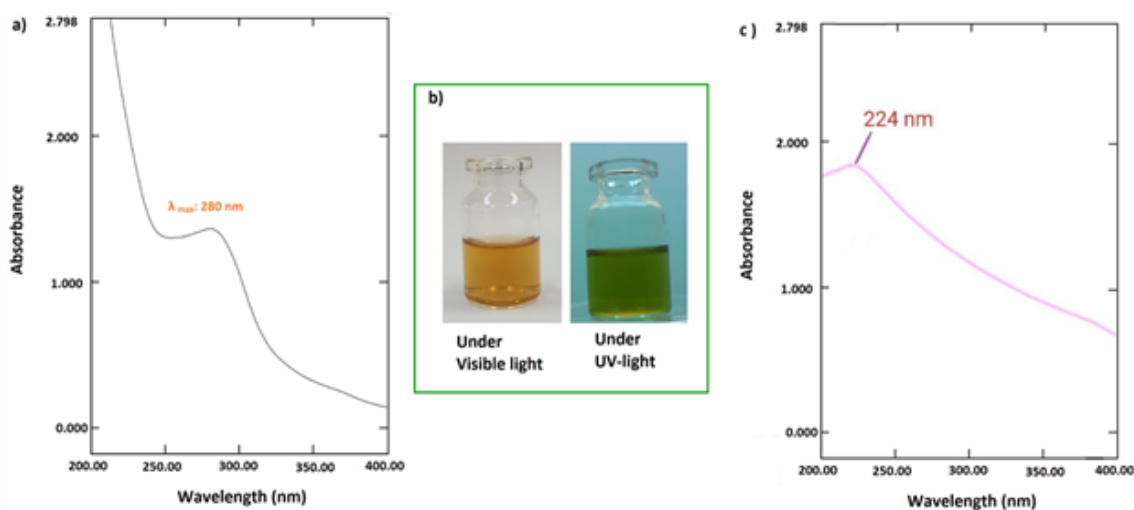


Fig. 4. (a) Absorption peak of C-QDs, (b) the optical images of the C-QDs solution synthesized under sunlight and UV (365 nm), and (c) the absorption spectrum of DNDs.

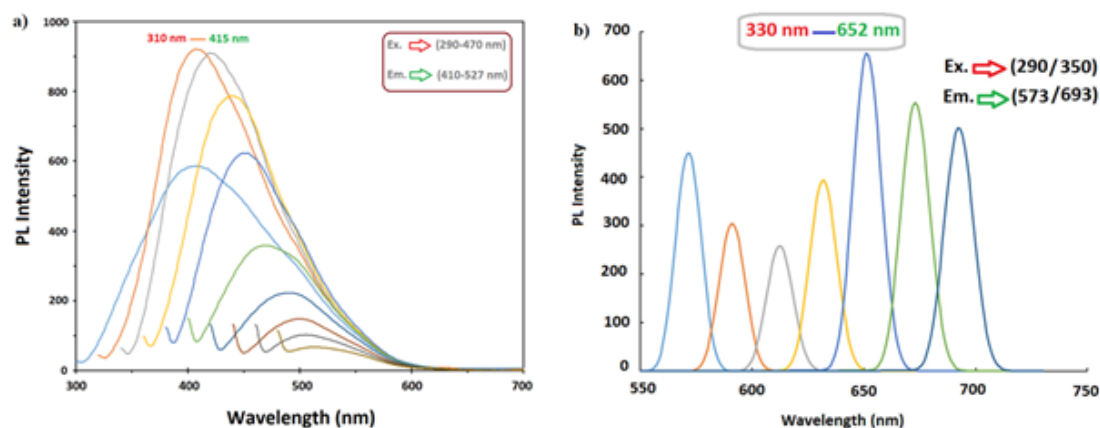


Fig. 5. (a) The emission spectra obtained at different excitation wavelengths and (b) the emission spectrum of DNDs.

of 200-400 nm regarding the DNDs suspension, which includes an absorption spectrum in the visible range with a wavelength of 224 nm [62]. The recorded absorption peak is related to the electron transfer of π - π^* type that the C=C groups may have caused.

Photo-Luminance

UV irradiation (365 nm) to the synthesized C-QD showed a green fluorescent reflection. The solution was lyophilized to investigate the optical behavior of the synthesized C-QD further. Subsequently, C-QDs solution (2000 $\mu\text{g}/\text{ml}$) was prepared to investigate the excitation wavelength at 290 to 470 nm. The maximum emission was observed at 415 nm with an excitation wavelength of 310 nm, while the emission peaks were shifted towards longer wavelengths (415 to 527 nm). In this regard, a good explanation would be the increased degree of oxygen-related oxidation and multiple functional groups on the surface of synthesized C-QDs caused by the extended surface-to-volume ratio. According to Fig. 5, the reduction of fluorescence emission in the obtained emission spectrum proves the tendency of C-QDs towards accumulation, which can be effective in fluorescence extinction. Therefore, the results of this photoluminescence confirm the presence of multiple functional groups and the small size of synthesized C-QDs, as the results of FTIR, XRD spectra, and UV-visible spectrophotometry also indicated. In addition, the absence of intrinsic PL in DNDs is caused by the electron transfers from the conduction layer to the valence layer, which can have variable PL amplitude and intensity depending on the size of DNDs [63]. Therefore,

the presence of functional groups on the surface of this product can induce changes in the fluorescence spectrum. So that, the presence of functional groups (hydroxyl, ketone, and ester) under the effect of excitation wavelength in the range of 290-350 nm led to the creation of an emission spectrum in the range of 573-693 nm. The photoluminescence analysis of DNDs indicated the maximum emission wavelength of 652 nm under the effect of an excitation wavelength of 330 nm. According to the research, there is not only an inverse relationship between the size of NDNs and the centres of nitrogen nuclei [64], but the observed fluorescence from DNDs in nano dimensions can produce a lower fluorescence intensity than nitrogen nuclei fluorescence [65].

Zeta potential

The synthesized C-QDs from chia seed origin displayed a negative zeta potential at high values. Fig. 6 a points out an increase in the value of zeta potential after the hydrothermal synthesis (-35.3 to -16.1 mV), which signifies the inducement of changes in the hydrocarbon chain pattern that converted the mucilage form into soluble C-QDs and resulted in surface charge alterations, while indicating the success of C-QDs synthesis as well. The colloidal stability of C-QDs was proved by their negative zeta potential in high values, which not only confirms the results of FTIR and XRD spectra in terms of claiming their excellent solubility but also guarantees the presence or usage of C-QDs in biological environments. We investigated the zeta potential of C-QDs particles labeled with a $^{99\text{m}}\text{Tc}$ radioisotope in the following. In conformity

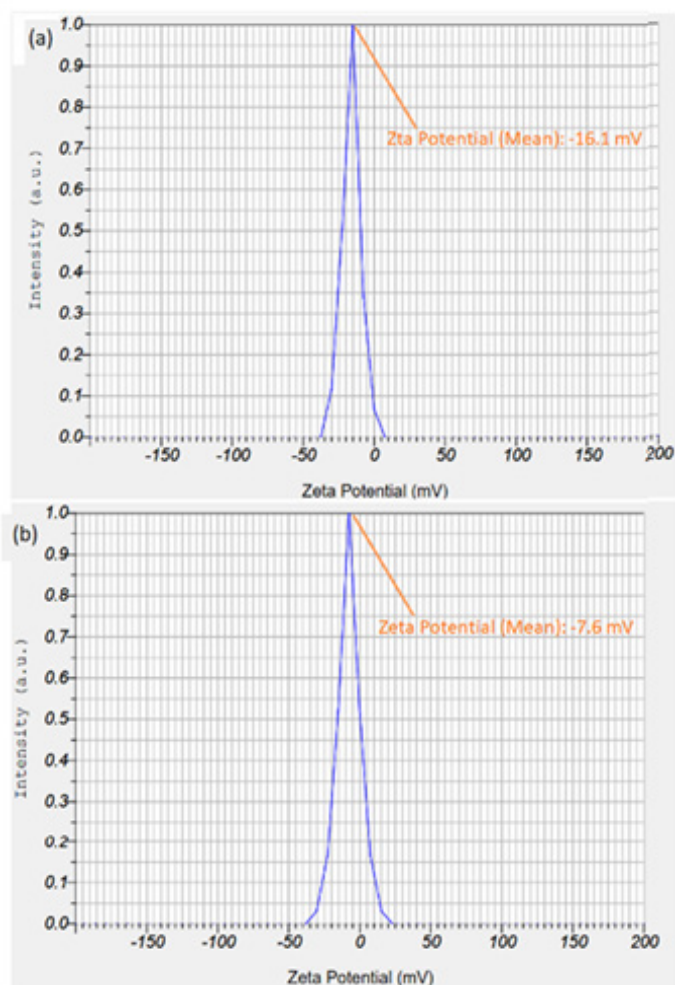


Fig. 6. (a) The ζ -potential reagents of synthesized C-QDs, and (b) ^{99m}Tc -C-QDs, respectively.

to Fig. 6b, ^{99m}Tc -C-QDs displayed a slight increase in their zeta potential value of -7.6 mV. However, the binding of ^{99m}Tc radioisotope to the surface of C-QDs was associated with a slight change in the negative zeta potential, which confirms the stable connection of ^{99m}Tc -C-QDs.

In total, the exertion of ^{99m}Tc -C-QDs can be suggested for targeted therapeutic and diagnostic purposes in clinical trials [66]. Also, the results reported a ζ -potential of 15.5 mV for the suspension of DNDs and a ζ -potential of 9.6 mV after the labeling process (^{99m}Tc -DNDs). Also, the colloidal stability of both states (suspension DNDs and ^{99m}Tc -DNDs) was confirmed due to the positive amount of exchange charge on the surface of DNDs, as well as the changes in the surface charge of ^{99m}Tc -DNDs in a decreasing manner. Therefore, bonding was successfully carried out due to

multiple functional groups on the surface of DNDs, which agrees with other characterizations such as FTIR and XRD. Furthermore, the average size of the hydrodynamic diameter of the particles (obtained from the diffusion coefficient by DLS technique) for CQDs and DNDs was 125 nm and 190 nm, respectively. Also, the average size of the hydrodynamic diameter of the obtained ^{99m}Tc -C-QDs and ^{99m}Tc -DNDs particles was determined with values of 1177 nm and 1680 nm, respectively. These results were obtained as the evaluation of dimer aggregations according to PDI was in the range of 0-1 [67, 68].

Microscopic evaluation

The crystal structure, size, and morphology of synthesized C-QDs can be observed in the two-dimensional image of Fig. 7a, which displays a

uniform distribution throughout the spherical morphologies of our product without any signs of aggregation. In conformity with Fig. 7, the histogram of synthesized C-QDs with a mean size was calculated at 4.9 ± 1.30 nm. Morphological and size parameters can determine the distribution and dispersion of C-QDs. Also, the obtained images exhibited the DNDs in the 10-15 nm range. In addition, the EDX outcomes contained the results of FTIR and XRD based on the degree of purity of DNDs with a high percentage of carbon when

compared to the other compatible elements.

Cytotoxicity assessment

Bioevaluation is conducted on the toxic properties of nanomaterials in various biomedical applications to check their potential effects on the health of humans and organisms [69]. MTT method (3-(4,5-dimethylthiazole-2-yl bromide)-2-diphenyltetrazolium) can provide the possibility of incubating cultured HEK293 and HepG2 cells (96 well plates, 5×10^3) with the specified concentration

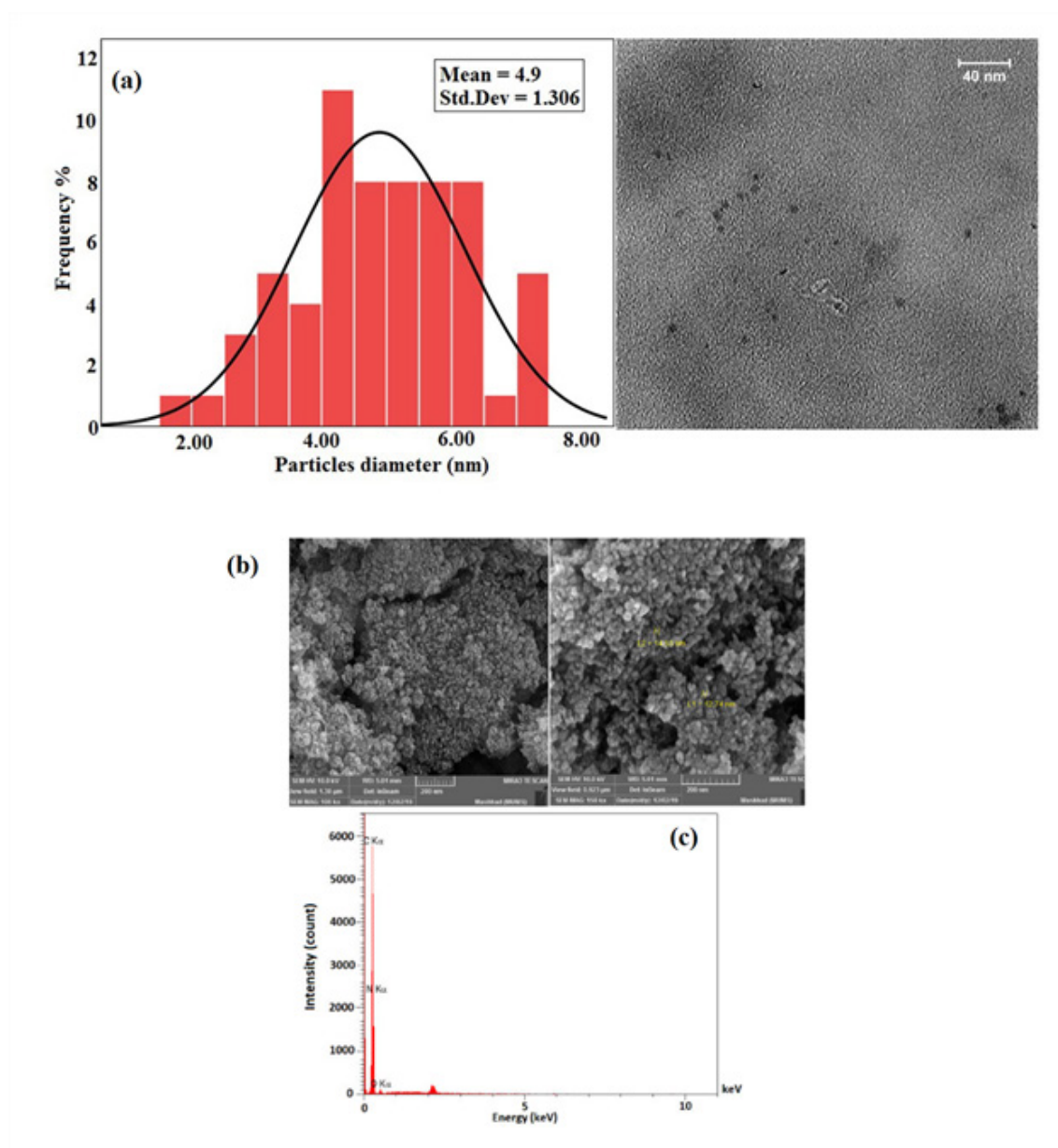


Fig. 7. (a) TEM and particle size distribution of prepared C-QDs and (b & c) FESEM and EDX images of DNDs.

range of C-QDs and DNDs (0, 15.5, 31.25, 62.5, 125, 250 and 500 $\mu\text{g/ml}$) for 48 h. According to Fig. 8, a negligible toxicity rate was observed at the concentration of 500 $\mu\text{g/ml}$ while achieving 90%< of survival for HEK293 cells in the presence of synthesized C-QDs from chia seeds. On the other hand, Fig. 8 presents the results of DNDs toxicity in the HepG2 cell line at the concentrations of 250 and 500 $\mu\text{g/ml}$, which displayed a slight decrease in the survival rate due to the presence of DNDs. The evaluation of the cytotoxic effects of synthesized C-QDs from plant sources and commercially bought DNDs showed their non-toxicity during *in vitro* studies, further supporting their potential for biomedical applications. According to the obtained IC50 from the MTT assay, an accurate biocompatibility assessment was performed by

incubating HEK293 and HepG2 cell lines near C-QDs and DNDs with the four concentrations for 48 h. The flow cytometry of studied nanoparticles was performed through the staining modification by V-FITC and PI [69]. Considering the results of the four areas, Q1 (necrosis), Q2 (late apoptosis), Q3 (early apoptosis), and Q4 (living cells) were analyzed in Fig. 8. Next to the lack of apoptosis in phase Q3 at the concentrations of 0, 62.5, 125 and 250 $\mu\text{g/ml}$, phase Q2 (250 $\mu\text{g/ml}$) showed a negligible percentage of apoptosis when compared to that of necrosis. The comparison of biocompatibility assessment of C-QDs and DNDs indicated their low sensitivity and dependence on the number of applied nanoparticles on HEK293 and HepG2 cell lines. In general, C-QDs and DNDs can be considered biocompatible nanomaterials

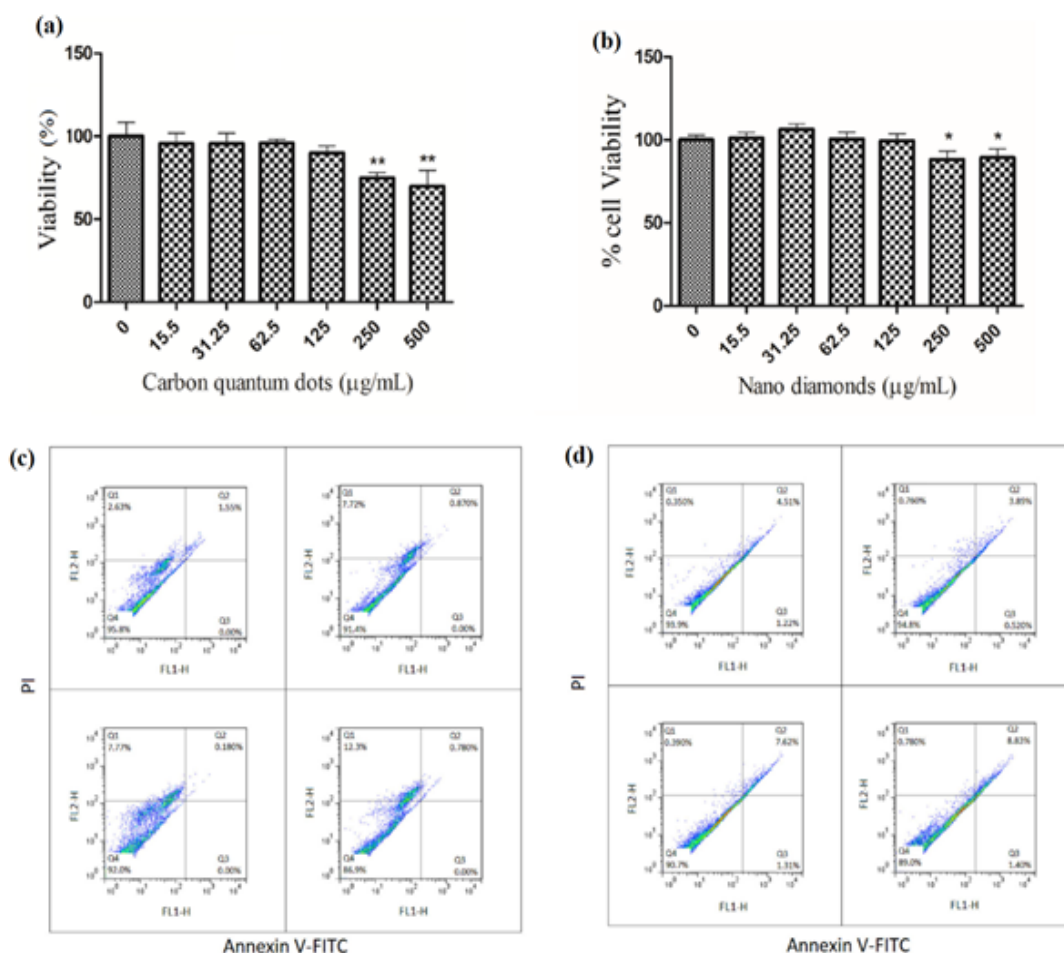


Fig. 8. (a) The cytotoxicity effects of C-QDs on HEK293 cell lines, (b) the cytotoxicity effects of DNDs on HepG2 cell lines for 48 h, (c) the flow-cytometry charts of C-QDs to evaluate biocompatibility on HEK293, and (d) the flow-cytometry charts of DNDs to evaluate biocompatibility on HepG2 cell lines.

exhibiting cellular interactions (as potential nanocarriers) in treatment and diagnosis.

Radiolabeling ^{99m}Tc -(C-QDs/DNDs)

We evaluated the quality of labeling by binding ^{99m}Tc radionuclide to the selected nanoparticles to investigate the colloidal stability of the labeled products. Instant thin layer chromatography (ITLC) can facilitate the possibility of assessing the optimal labeling of nanoparticles with the help of radiopharmaceuticals in two reservoirs of acetone and ethanol throughout the time intervals of 0, 1, 4, and 24 h. In this test, the fixed phase of ITLC (Silica gel paper) was settled at the beginning of the 5.0 μl staining strip. The studied media were technetium-labeled nanoparticles for separately assessing the factors of colloidal stability, human serum, and double distilled water. Then, a silica gel strip containing the stain was placed inside the acetone and ethanol tanks for the required period. Once the silica gel strips were cut into three equal parts, they were placed in separate tubes for gamma counter position to read the radioactivity. The efficiency of colloidal stability evaluated by ITLC for ^{99m}Tc -C-QDs in human serum and double distilled water systems at regular intervals was 98% and 93%, respectively. The results of detecting the ^{99m}Tc -C-QDs in acetone phases and the 85% methanol solvent for 24 h showed 92% and 93% stability for the distilled water system, respectively, while the human serum system displayed a superior percentage of 98% of colloidal stability level. In addition, the study of ζ potential for negative charge changes at the level of C-QDs and ^{99m}Tc -C-QDs forms indicated the binding of ^{99m}Tc radioisotope to the surface of C-QDs. In the subsequent study (^{99m}Tc -DNDs), the colloidal stability efficiency of ^{99m}Tc radioisotope binding in double-distilled underwater media and

human serum was 99% and 98%, respectively. According to ζ -potential analysis, a decrease in electrostatic forces was observed after binding to the DNDs surface. Two studies on ^{99m}Tc -C-QDs and ^{99m}Tc -DNDs in acetone and ethanol showed 85% colloidal stability. The results are presented in table 1 and 2.

In-vitro stability study

We determined the binding of ^{99m}Tc -nanoparticles (^{99m}Tc -C-QDs, ^{99m}Tc -DNDs) to the cells (HEK293 and HepG2) at the concentrations of 30 and 90 $\mu\text{g}/\text{ml}$ per cell of the 6-well plate, respectively, which were added to the cell lines in three replications to be incubated at the specified time intervals (3-4 h) [70]. Subsequently, the samples were washed and replaced with fresh PBS to remove the ^{99m}Tc -free nanoparticles. The measurement of γ rays was completed by transferring the contents of each well into the special tubes of the gamma counter device. According to the results, the binding effects of ^{99m}Tc -C-QDs and ^{99m}Tc -DNDs were observed at the low concentrations of 50% and 40%, respectively, obtained cell binding efficiencies at a concentration of 90 $\mu\text{g}/\text{ml}$ were 18% and 15%, respectively. Evidence shows that increasing the spherical and hemispherical concentration and morphology can be a favourable factor in the intracellular adsorption of small nanoparticles (C-QDs and DNDs). In general, the interaction of hydroxyl terminals among the studied nanoparticles with HEK293 and HepG2 cell membranes displayed a worthy binding efficiency at a concentration of 30 $\mu\text{g}/\text{ml}$ (low concentration).

In-vivo biodistribution

Bioaccumulation was carried out in rats via intravenous injection to confirm the cytotoxicity

Table 1. Stability efficiency assessment of ^{99m}Tc -C-QDs at intervals of 0, 1, 4, and 24 h.

Labeling stability of ^{99m}Tc -C-QDs (%)	Incubation times (h) in D2W				Incubation times (h) in human serum			
	0	1	4	24	0	1	4	24
Acetone	84	88	92	91	94	95	93	98
Methanol	95	95	96	93	74	78	95	96

Table 2. Stability efficiency assessment of ^{99m}Tc -DNDs at intervals of 0, 1, 4, and 24 h.

Labeling stability of ^{99m}Tc -DNDs (%)	Incubation times (h) in D2W				Incubation times (h) in human serum			
	0	1	4	24	0	1	4	24
Acetone	97	99	97	99	99	99	98	98
Methanol	95	98	93	94	97	99	96	97

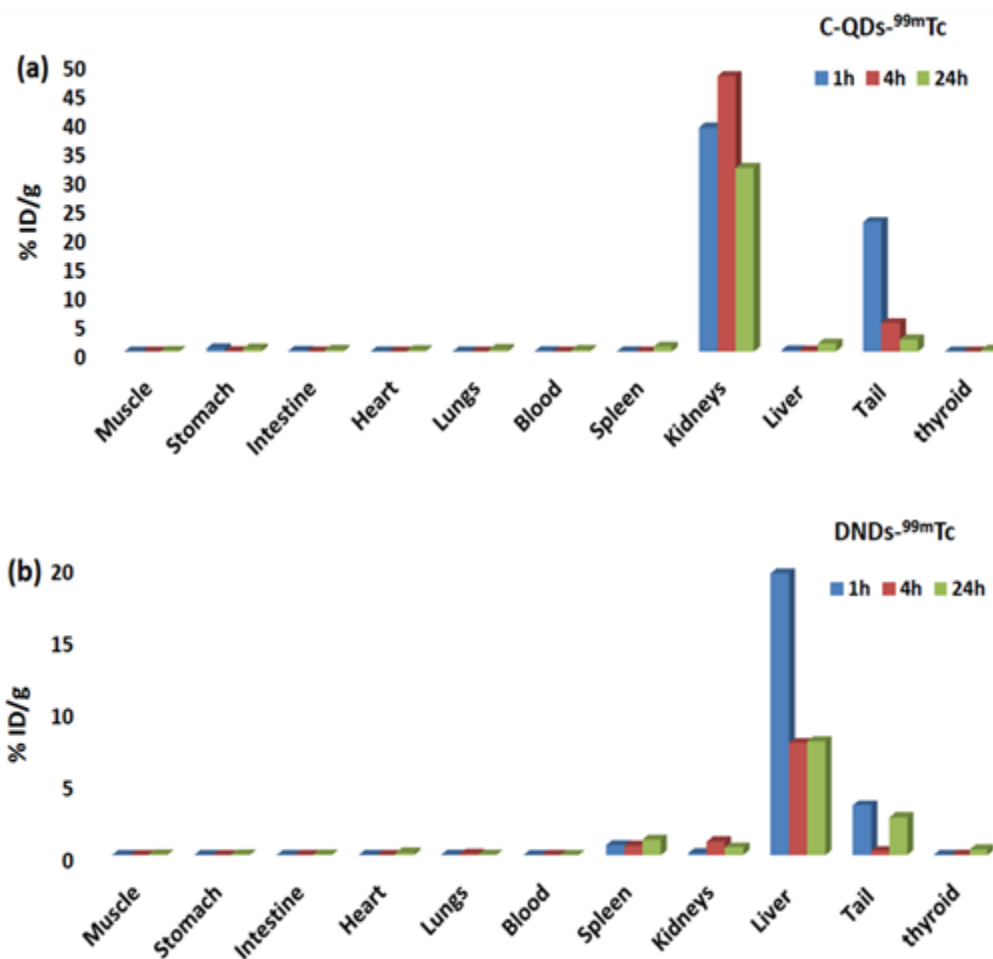


Fig. 9. (a) The bio-distribution of ^{99m}Tc -C-QDs and (b) ^{99m}Tc -DNDs in rats at 1, 4 and 24 h.

and quality control tests of ^{99m}Tc -C-QDs and ^{99m}Tc -DNDs. The basis of this study is the estimation of radioactive uptake into any organism's tissues (%ID/g) [71]. According to previous investigations, this study involved three groups with three replications sacrificed at regular intervals (1, 4, and 24 h) after an intravenous injection through the rats' tails. To estimate the emitted γ -photons, the isolated limbs were placed in the special tubes of the gamma counter to be placed in the γ -photon reading position of the counter. According to the results, the maximum radioactive absorption of ^{99m}Tc -C-QDs, and ^{99m}Tc -DNDs was observed in kidney and liver tissues, respectively. Biodistribution studies indicated the accumulation of C-QDs in kidney tissues at approximately 48% along with the amount of ^{99m}Tc , the liver stood in the second place of biological distribution with 1.5%, and the thyroid was estimated to be the

least radioactive absorbing organ with a value of 0.3%. In addition, causing a reduction in the hydrophobic and ionic interactions of ^{99m}Tc -C-QDs with the cell membrane surface, induced by the labeling process, resulted in a decrease in the immune system response and increased circulation time of the body. Therefore, it can be considered an ideal candidate in terms of retention time in the kidney tissue for centralized imaging and treatment purposes [72]. Despite the reduction in the amount of radioactive radiation of liver tissue during the experiment, the evaluation of ^{99m}Tc -DNDs resulted in 19% uptake when compared to other tissues, especially spleen tissues with 1.5% and kidneys by 0.93% (second and third places), respectively. Supplementary calculations indicated the lung and thyroid organs as the lowest selected organs of ^{99m}Tc -DNDs bioaccumulation with values of .1% and 0.5%. The bioaccumulation outcomes

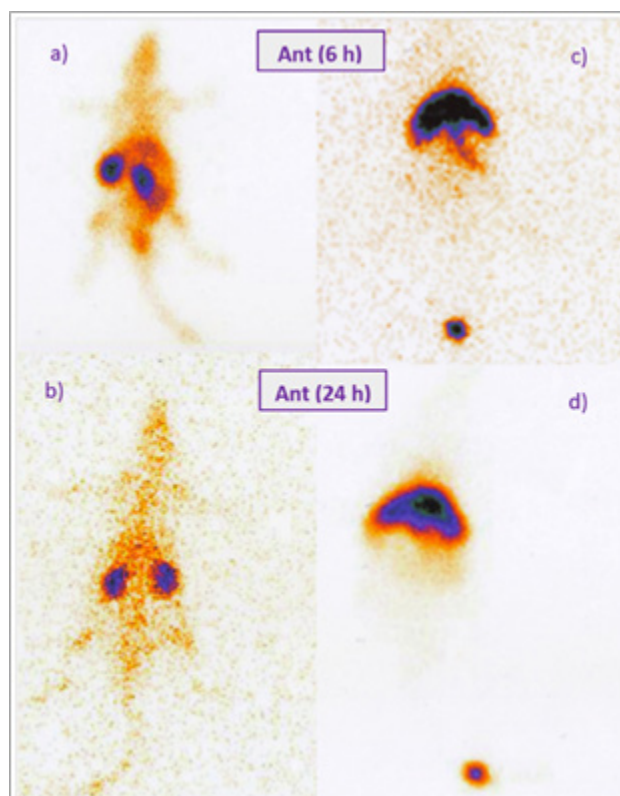


Fig. 10. The anterior images (6 and 24 h; a & b) of ^{99m}Tc -C-QDs; and (c & d) corresponding to ^{99m}Tc -DNDs.

(^{99m}Tc -C-QDs and ^{99m}Tc -DNDs) were observed according to Fig. 9. The presence of ^{99m}Tc -nanoparticles can prove their stability and optimal permeability due to the tendency of labeled nanoparticle surfaces towards kidney and liver tissue cells.

Bioimaging

The bioimaging evaluation of ^{99m}Tc -labeled nanoparticles (^{99m}Tc -C-QDs, and ^{99m}Tc -DNDs) began with randomly selecting one of the three rats in the group 24 h after injecting ^{99m}Tc -labeled nanoparticles. Subsequently, the rats were anesthetized by subcutaneous injection (ketamine and xylazine), while the images were taken 6 and 24 h after the injection. The obtained images of ^{99m}Tc -C-QDs and ^{99m}Tc -DNDs confirmed the results of the biological distribution of kidney and liver organs, respectively. The biodistribution of ^{99m}Tc -C-QDs is displayed in Fig. 10 in sections (a & b) and ^{99m}Tc -DNDs in sections (c, d) throughout the anterior state at 6 and 24 h after the intravenous injection of rats.

CONCLUSION

This study was performed based on the

similarity of physicochemical properties of carbon sources (C-QDs and DNDs) under *in vivo* (rats) and *in vitro* evaluation. The similarity of obtained results for the characterization of C-QDs (with plant source chia seeds) and DNDs (purchased as a commercial sample) was confirmed. The reported sizes by TEM and FESEM analysis are visible throughout the images, in the range of <10 nm with spherical and semi-spherical morphology. Moreover, the results of XRD analysis confirm the amorphous structure in C-QDs and DNDs due to the presence of SP3 molecular orbitals. Also, EDX analysis confirmed a high degree of purity of DNDs for competitive analysis with C-QDs. Other features, such as excellent solubility, optical properties (especially in C-QDs) (caused by their quantum properties), non-toxicity, and biocompatibility, issued their necessary permission to be applied in the *in vivo* studies of rats. In general, the biodistribution of ^{99m}Tc -C-QDs and ^{99m}Tc -DNDs indicated that despite the similar physico-chemical features of C-QDs and DNDs, they may exhibit different bioaccumulation and tendencies towards an organ of a unit. The presence of functional groups at the level of C-QDs and DNDs can become one of the intervening factors for creating concentrated tendencies in

C-QDs and DNDs towards organs. On the other hand, the size and morphology of C-QDs and DNDs proved effective in terms of the intracellular diffusion coefficient and the duration of intrabody retention. In conclusion, C-QDs and DNDs should be used as carbon sources-based nanoparticles in chemotherapy research and targeted imaging.

ETHICAL COMPLIANCE

Research experiments conducted in this article with animals or humans were approved by the Ethical Committee and responsible authorities of our research organization (s) following all guidelines, regulations, and legal and ethical standards as required for humans or animals.

CONFLICTS OF INTEREST

There are no conflicts to declare.

ACKNOWLEDGMENTS

The authors appreciate all the technical support Mashhad University of Medical Sciences provided.

REFERENCES

- Ahmed S, Ikram S. Biosynthesis of gold nanoparticles: a green approach. *J Photochem Photobiol B*. 2016;161:141-153.
- Diederich F, Rubin Y. Synthetic approaches toward molecular and polymeric carbon allotropes. *Angew Chem Int Ed Engl*. 1992;31(9):1101-1123.
- Kumar SA, Jarvin M, Inbanathan SSR, Umar A, Lalla NP, Dzade NY, et al. Facile green synthesis of magnesium oxide nanoparticles using tea (*Camellia sinensis*) extract for efficient photocatalytic degradation of methylene blue dye. *Environ Technol Innov*. 2022;28:102746.
- Arenal R, Lopez-Bezanilla A. Boron nitride materials: an overview from 0D to 3D (nano) structures. *Wiley Interdisciplinary Reviews: Comput Mol Sci*. 2015;5(4):299-309.
- Santana-Mayor Á, Rodríguez-Ramos R, Socas-Rodríguez B, Asensio-Ramos M, Rodríguez-Delgado MÁ. Carbon-based adsorbents. *SPE*. 2020; 83-127.
- Saleh TA. Nanomaterials: Classification, properties, and environmental toxicities. *Environ Technol Innov*. 2020;20:101067.
- Cordill MJ, Weinberger CR. Mechanical Behavior at the Nanoscale: What's in your Toolbox? *JOM*. 2018;70(7):1065-1067.
- Wang H, O'Leary S. Electromagnetically induced transparency from electron spin coherences in semiconductor quantum wells. *JOSA B*. 2012;29(2):A6-A16.
- Brand C, Pfnür H, Landolt G, Muff S, Das T, Tegenkamp C. Observation of correlated spin-orbit order in a strongly anisotropic quantum wire system. *Nat Commun*. 2015;6(1):1-7.
- Li J, Yun X, Hu Z, Xi L, Li N, Tang H, et al. Three-dimensional nitrogen and phosphorus co-doped carbon quantum dots/reduced graphene oxide composite aerogels with a hierarchical porous structure as superior electrode materials for supercapacitors. *J Mater Chem A*. 2019;7(46):26311-6325.
- Molaei MJ. A review on nanostructured carbon quantum dots and their applications in biotechnology, sensors, and chemiluminescence. *Talanta*. 2019;196:456-478.
- Janus Ł, Radwan-Pragłowska J, Piątkowski M, Bogdał D. Facile synthesis of surface-modified carbon quantum dots (CQDs) for biosensing and bioimaging. *Mater*. 2020;13(15):3313.
- Karami MH, Abdouss M. Recent advances of carbon quantum dots in tumor imaging. *Nanomed J*. 2024;11(1):13-35.
- Mehra NK, Jain NK. Multifunctional hybrid-carbon nanotubes: new horizon in drug delivery and targeting. *J Drug Target*. 2016;24(4):294-308.
- Zou F-R, Wang S-N, Wang F-F, Liu D, Li Y. Synthesis of lanthanide-functionalized carbon quantum dots for chemical sensing and photocatalytic application. *Catal*. 2020;10(8):833.
- Velayati M, Hassani H, Sabouri Z, Mostafapour A, Darroudi M. Green-based biosynthesis of Se nanorods in chitosan and assessment of their photocatalytic and cytotoxicity effects. *Environ Technol Innov*. 2022;27:102610.
- Liang X, Li N, Zhang R, Yin P, Zhang C, Yang N, et al. Carbon-based SERS biosensor: From substrate design to sensing and bioapplication. *NPG Asia Mater*. 2021;13(1):1-36.
- Hsiao P-H, Timjan S, Kuo K-Y, Juan J-C, Chen C-Y. Optical management of CQD/AgNP@ SiNW arrays with highly efficient capability of dye degradation. *Catal*. 2021;11(3):399.
- Vo NTT, You S-J, Pham M-T, Pham VV. A green synthesis approach of p-n CuO/ZnO junctions for multifunctional photocatalysis towards the degradation of contaminants. *Environ Technol Innov*. 2023;32:103285.
- Ying S, Guan Z, Ofoegbu PC, Clubb P, Rico C, He F, Hong J. Green synthesis of nanoparticles: Current developments and limitations. *Environ Technol Innov*. 2022;26:102336.
- Tajik S, Dourandish Z, Zhang K, Beitollahi H, Van Le Q, Jang HW, Shokouhimehr M. Carbon and graphene quantum dots: A review on syntheses, characterization, biological and sensing applications for neurotransmitter determination. *RSC Adv*. 2020;10(26):15406-15429.
- Mandal P, Ghosh SK, Grewal HS. Graphene oxide coated aluminium as an efficient antibacterial

- surface. *Environ Technol Innov.* 2022;28:102591.
23. Galeas S, Valdivieso-Ramírez CS, Pontón PI, Guerrero VH, Goetz V. Photocatalytic degradation of phenol under visible light irradiation by using ferrous oxalate synthesized from iron-rich mineral sands via a green hydrothermal route. *Environ Technol Innov.* 2023;32:103325.
 24. Permatasari FA, Irham MA, Bisri SZ, Iskandar F. Carbon-based quantum dots for supercapacitors: Recent advances and future challenges. *Nanomater.* 2021;11(1):91.
 25. Bak S, Kim D, Lee H. Graphene quantum dots and their possible energy applications: A review. *Curr Appl Phys.* 2016;16(9):1192-1201.
 26. Rahbar M, Mehrzad M, Behpour M, Mohammadi-Aghdam S, Ashrafi M. S, N co-doped carbon quantum dots/TiO₂ nanocomposite as highly efficient visible light photocatalyst. *Nanotechnol.* 2019;30(50):505702.
 27. Shao B, Liu Z, Zeng G, Wang H, Liang Q, He Q, et al. Two-dimensional transition metal carbide and nitride (MXene) derived quantum dots (QDs): synthesis, properties, applications and prospects. *J. Mater Chem A.* 2020;8(16):7508-7535.
 28. Dager A, Baliyan A, Kurosu S, Maekawa T, Tachibana M. Ultrafast synthesis of carbon quantum dots from fenugreek seeds using microwave plasma enhanced decomposition: application of C-QDs to grow fluorescent protein crystals. *Sci Rep.* 2020;10(1):1-15.
 29. Robertson J. Gap states in diamond-like amorphous carbon. *Philos Mag B.* 1997;76(3):335-350.
 30. Tiwari SK, Kumar V, Huczko A, Oraon R, Adhikari AD, Nayak G. Magical allotropes of carbon: prospects and applications. *Crit Rev Solid State Mater Sci.* 2016;41(4):257-317.
 31. Hu M, Zhao Z, Tian F, Oganov AR, Wang Q, Xiong M, et al. Compressed carbon nanotubes: a family of new multifunctional carbon allotropes. *Sci Rep.* 2013;3(1):1-7.
 32. Fedortchouk Y. A new approach to understanding diamond surface features based on a review of experimental and natural diamond studies. *Earth-Sci Rev.* 2019;193:45-65.
 33. Cheng F, Jiang S. Cavitation erosion resistance of diamond-like carbon coating on stainless steel. *Appl Surf Sci.* 2014;292:16-26.
 34. Xu C, He D, Wang H, Guan J, Liu C, Peng F, et al. Nanopolycrystalline diamond formation under ultra-high pressure. *IJRMHM.* 2013;36:232-237.
 35. Suga Y, Watanabe T. Plasma optical emission spectroscopy in supercritical fluid for material synthesis process. *MRS-J.* 2010;35(1):15-27.
 36. Daulton T, Kirk M, Lewis R, Rehn L. Production of nanodiamonds by high-energy ion irradiation of graphite at room temperature. *Nucl Instrum Methods Phys Res B.* 2001;175:12-20.
 37. Jia S, Zhang D, Xuan Y, Nastac L. An experimental and modeling investigation of aluminum-based alloys and nanocomposites processed by ultrasonic cavitation processing. *Appl Acoust.* 2016;103:226-231.
 38. Angus JC. Diamond synthesis by chemical vapor deposition: The early years. *Diam Relat Mater.* 2014;49:77-86.
 39. Fahrenholtz WG. Detonation Synthesis of Nanomaterials. Missouri S&T. 2017.
 40. Yang N. Novel aspects of diamond. *Topics in Applied Physics Springer International Publishing, Cham.* 2015.
 41. Mochalin V, Shenderova O, Ho D, Gogotsi Y. The properties and applications of nanodiamonds. *Nano-Enabled Medical Applications.* 2020:313-350.
 42. Shukla A, Parmar P, Saraf M. Radiation, radionuclides and bacteria: An in-perspective review. *J Environ Radioact.* 2017;180:27-35.
 43. Skowron K. Properties of the nanocrystalline layers obtained by methods of severe plastic deformation in metals and alloys for biomedical applications. 2021.
 44. Hodayun B, Lin X, Choi H-J. Challenges and recent progress in oral drug delivery systems for biopharmaceuticals. *Pharmaceutics.* 2019;11(3):129.
 45. Kesharwani P, Ghanghoria R, Jain NK. Carbon nanotube exploration in cancer cell lines. *Drug Discov Today.* 2012;17(17-18):1023-1030.
 46. Teow Y, Valiyaveetil S. Active targeting of cancer cells using folic acid-conjugated platinum nanoparticles. *Nanoscale.* 2010;2(12):2607-2613.
 47. Yang L, Liu B, Ye Z, Yang C, Wang Z, Chen B, et al. Investigation into surface composition of nitrogen-doped niobium for superconducting RF cavities. *Nanotechnology.* 2021;32(24):245701.
 48. Herrmann K, Schwaiger M, Lewis JS, Solomon SB, McNeil BJ, Baumann M, et al. Radiotheranostics: a roadmap for future development. *Lancet Oncol.* 2020;21(3):e146-e156.
 49. Miranda SEM. Evaluation of lapachol radiolabeled with Technetium-99m as tumoral marker and development and characterization of nanoemulsion containing lapachol.
 50. de Barros ALB, Cardoso VN, das Graças Mota L, Alves RJ. Synthesis and biodistribution studies of carbohydrate derivatives radiolabeled with technetium-99m. *BMCL.* 2010;20(1):307-315.
 51. Dilworth J, Parrott S. The biomedical chemistry of technetium and rhenium. *Chem Soc Rev.* 1998;27(1):43-55.
 52. Madru R, Kjellman P, Olsson F, Wingårdh K, Ingvar C, Ståhlberg F, et al. 99mTc-labeled superparamagnetic iron oxide nanoparticles for multimodality SPECT/MRI of sentinel lymph nodes. *J. Nucl Med.* 2012;53(3):459-463.
 53. Narra VR, Sastry KS, Goddu SM, Howell RW, Strand SE, Rao DV. Relative biological effectiveness

- of ^{99m}Tc radiopharmaceuticals. *Med Phys.* 1994;21(12):1921-1926.
54. Wang Y, Xu C, Ow H. Commercial nanoparticles for stem cell labeling and tracking. *Theranostics.* 2013;3(8):544.
 55. Kamelnia E, Divsalar A, Darroudi M, Yaghmaei P, Sadri K. Synthesis, ^{99m}Tc-radiolabeling, and biodistribution of new cellulose nanocrystals from *Dorema kopetdaghensis*. *Int J Biol Macromol.* 2020;146:299-310.
 56. Nemati S, Hosseini HA, Hashemzadeh A, Mohajeri M, Sabouri Z, Darroudi M, Oskuee RK. Cytotoxicity and photocatalytic applications of biosynthesized ZnO nanoparticles by *Rheum turketanicum* rhizome extract. *Mater Res Express.* 2019;6(12):125016.
 57. Thongsai N, Supchocksoonthorn P, Dwyer JH, Wei W, Sun J, Gopalan P, Paoprasert P. High-capacity adsorbent/sensor from nylon 6 derived carbon dots on SiO₂ substrate via one-step surface grafting. *Mater Sci Eng B.* 2020;262:114692.
 58. Sadri K, Ren Q, Zhang K, Paudyal B, Devadhas D, Rodeck U, Thakur M. PET imaging of EGFR expression in nude mice bearing MDA-MB-468, a human breast adenocarcinoma. *Nucl Med Commun.* 2011;32(7):563-569.
 59. Gubin S, Popkov O, Yurkov GY, Nikiforov V, Koksharov YA, Eremenko N. Magnetic nanoparticles fixed on the surface of detonation nanodiamond microgranules. *Diam Relat Mater.* 2007;16(11):1924-1928.
 60. Walekar LS, Zheng M, Zheng L, Long M. Selenium and nitrogen co-doped carbon quantum dots as a fluorescent probe for perfluorooctanoic acid. *Mikrochim Acta.* 2019;186(5):1-9.
 61. Souza da Costa R, Ferreira da Cunha W, Simenremis Pereira N, Marti Ceschin A. An Alternative Route to Obtain Carbon Quantum Dots from Photoluminescent Materials in Peat. *Mater.* 2018;11(9):1492.
 62. Durazzo A, Kiefer J, Lucarini M, Camilli E, Marconi S, Gabrielli P, et al. Qualitative analysis of traditional Italian dishes: FTIR approach. *Sustainability.* 2018;10(11):4112.
 63. Fuente E, Menendez J, Suarez D, Montes-Morán M. Basic surface oxides on carbon materials: a global view. *Langmuir.* 2003;19(8):3505-3511.
 64. Amjadi M, Hallaj T, Asadollahi H, Song Z, de Frutos M, Hildebrandt N. Facile synthesis of carbon quantum dot/silver nanocomposite and its application for colorimetric detection of methimazole. *Sens Actuators B: Chem.* 2017;244:425-432.
 65. Chung P-H, Perevedentseva E, Cheng C-L. The particle size-dependent photoluminescence of nanodiamonds. *Surf Sci.* 2007;601(18):3866-3870.
 66. Liu ML, Chen BB, Li CM, Huang CZ. Carbon dots: synthesis, formation mechanism, fluorescence origin and sensing applications. *Green Chem.* 2019;21(3):449-471.
 67. Yuk SB, Lee JM, Namgoong JW, Sakong C, Hwang TG, Kim SH, et al. Synthesis of bay-linked perylene dimers with enhanced solubility for high optical density black matrix material. *Dyes Pigm.* 2019;171:107695.
 68. Doherty MW, Manson NB, Delaney P, Jelezko F, Wrachtrup J, Hollenberg LC. The nitrogen-vacancy colour centre in diamond. *Phys Rep.* 2013;528(1):1-45.
 69. Hossein Banazadeh M, Saidi MS, Firoozabadi B. Numerical Analysis of Flow and Mass Transfer in the Renal Glomeruli Capillary Network. *Modares Mech Eng.* 2014;14(8).
 70. Moffat D, Fourman J. The vascular pattern of the rat kidney. *J Anat.* 1963;97(Pt 4):543.
 71. Nazarkovsky M, de Mello HL, Bisaggio RC, Alves LA, Zaitsev V. Hybrid suspension of nanodiamonds-nanosilica/titania in cytotoxicity tests on cancer cell lines. *Inorg Chem Commun.* 2020;111:107673.
 72. Mahmoud KA, Mena JA, Male KB, Hrapovic S, Kamen A, Luong JH. Effect of surface charge on the cellular uptake and cytotoxicity of fluorescent labeled cellulose nanocrystals. *ACS Appl Mater Interfaces.* 2010;2(10):2924-2932.